

ARTICLE OPEN



Corrosion of ternary borosilicate glass in acidic solution studied in operando by fluid-cell Raman spectroscopy

Christoph Lenting^{1,2} and Thorsten Geisler¹

Fluid-cell Raman spectroscopy is a space and time-resolving application allowing in operando studies of dynamic processes during solution–solid interactions. A currently heavily debated example is the corrosion mechanism of borosilicate glasses, which are the favoured material for the immobilization of high-level nuclear waste. With an upgraded fluid-cell lid design made entirely from the glass sample itself, we present the polymerization of the surface alteration layer over time in an initially acidic environment, including the differentiation between pore and surface-adsorbed water within it. Our results support an interface-coupled dissolution-precipitation model, which opposes traditional ion-exchange models for the corrosion mechanism. A sound description of the corrosion mechanism is essential for reliable numerical models to predict the corrosion rate of nuclear waste glasses during long-term storage in a geological repository.

npj Materials Degradation (2021)5:37; <https://doi.org/10.1038/s41529-021-00182-5>

INTRODUCTION

Corrosion studies are commonly conducted in a multi-step fashion, involving first the alteration experiment itself, followed by sample preparation, and post mortem analysis. Inherently, structural and chemical changes due to the preparation step have to be considered when interpreting the post-mortem analysis. In general, post mortem analysis suffers from two major disadvantages: (1) quenching, i.e., sudden change of environmental conditions from the termination of the experiment and subsequent drying, sawing, and polishing may alter the structure of the corrosion product and (2) the quenched sample represents only one point in time in a dynamic process of potentially multiple reaction steps. For post-mortem analysis, the latter can only be overcome by performing several experiments in parallel and quenching these at different time steps, making it difficult to correlate textural observations as new samples have to be used for each time step.

Specifically for silicate glass corrosion, quenching and drying the sample is critical as the main corrosion product is a hydrous amorphous silica gel (e.g., see refs. ^{1–3} and references therein), which is generally prone to structural and chemical changes such as condensation and/or polymerization, loss of water, and/or cracking due to cooling, changes in pH, and dehydration⁴. Surface coatings of secondary minerals, which are common phenomena observed with chemically more complex glass or solution composition (e.g., see ref. ⁵), could to some extent be the result of rapid supersaturation by quenching the experiment to room temperature. This has to be taken into account in the ongoing discussion about the role of secondary mineral precipitates for the potential corrosion rate resumption in long-term disposal scenarios of vitrified high-level nuclear waste⁶.

Based on a number of the recent experimental studies utilizing isotope tracer analyses^{3,7–11}, high-resolution TEM imaging^{11–13}, and atom probe tomography¹⁴, the overall mechanistic framework of silicate glass corrosion has been questioned. Thus, in situ studies overcoming the above-mentioned shortcomings of post-mortem analyses might become essential for the formulation of a

coherent corrosion mechanism. However, only a limited number of analytical techniques are available that allow studying solid–water reactions in operando without disturbing the reaction.

In the last decades, atomic force microscopy (AFM) has as in situ technique become a vital tool for the in situ study of mineral surfaces in contact with aqueous solution at ambient^{15,16} and even at elevated temperatures up to 150 °C¹⁷. However, it is by design limited to morphological changes at the surface of the solid of interest, which is not applicable to study the evolution of a surface alteration layer (SAL) as needed for the simulation of long-term storage of corrosion-resistant glasses. Hence, only few studies used this in situ technique, e.g. see refs. ^{18,19}. Vertical scanning interferometry (VSI) is another surface-related analytical technique. It can provide dissolutions rates of a specific surface based on minute height measurements in relation to a masked reference surface²⁰ and was also successfully applied for the study of glass corrosion²¹. However, similar to AFM, VSI can only record the dissolution of a surface until a layer of a secondary phase precipitates. Another disadvantage of this technique is the necessity to interrupt the experiment and dry samples for the height measurements.

The development of silica-based alteration layers on minerals has recently been analysed up to 80 °C by in situ synchrotron-based X-ray reflectivity, which allows to directly monitor dissolution and growth rates of the mineral and surface layer as well as infer structural properties of these layer from the scattering length density²².

A different in situ approach is the in situ measurement of ions and pH with microelectrodes in solution during experimental corrosion/alteration on wollastonite (CaSiO₃)²³ that was used to investigate the reaction dynamics and formation of amorphous silica layers as corrosion product. However, the ‘open reactor’ design limits the applicability to ambient temperatures and relative short run times. Nonetheless, the study makes as strong case for the reaction being governed by the formation of strong solute concentration gradients between the corroding interface and the bulk solution, which is arguably transferable to the

¹Institut für Geowissenschaften, Rheinische Friedrich-Wilhelms-Universität Bonn, Bonn, Germany. ²Institut für Geologie und Mineralogie, Universität zu Köln, Köln, Germany. ✉email: c.lenting@uni-koeln.de

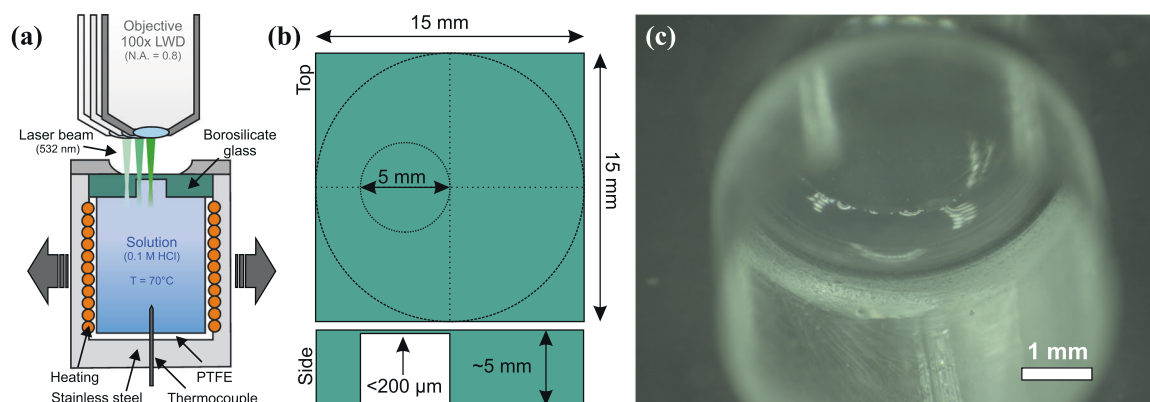


Fig. 1 **Experimental setup.** **a** Schematic of fluid cell. For illustration, relative movement between objective and fluid cell is presented here, while in reality the objective is fixed to the microscope, and the XYZ stage, on which the fluid cell is mounted, is the only moving part. **b** Schematic of glass lid with dimensions. **c** Micrograph taken from the bottom of the glass cuboid into the blind hole.

corrosion of silicate glasses as well. The only major in situ data regularly obtained during glass corrosion experiments are aliquot analyses of the bulk solution, which are, however, less meaningful when discussing the underlying corrosion mechanisms, particularly in the light of the above-mentioned findings.

In a recent paper²⁴, fluid cell Raman spectroscopy was applied for the first time to investigate the glass corrosion progress in operando, i.e., resolved in space and time. With a lateral resolution of about $10 \mu\text{m}$ and time-step size of about 1.5 h per linescan, it was possible to show corrosion rate changes, the built-up of a pH gradient at the solution–glass interface as well as within the SAL. The glass (60% SiO_2 , 20% B_2O_3 , 20% Na_2O) was altered under a near neutral pH, revealing the formation of a several-micrometre-thick water-rich zone between the SAL and the glass, which was interpreted as an interface solution, as well as pH gradients at the glass surface and within the SAL. Furthermore, by replacing the running solution with a deuterated solution without terminating the experiment, it could be shown that water transport through the SAL cannot be the rate-limiting step for the corrosion process. Encouraged by these results, we lightly refined the cell design to improve the spatial and depth resolution by eliminating refraction interfaces. For this purpose, the entire lid of the fluid cell was manufactured from the same sample glass with a sink hole drilled from the bottom functioning as reaction interface (Fig. 1). Note here that this is, of course, only a viable option for other transparent amorphous or crystalline materials if ample material of a single body is available. Lastly, an acidic reaction solution was chosen to complement the results of the previous in operando study²⁴ and to test whether an interface-coupled dissolution-precipitation process (ICDP) also operates in acidic solutions, as suggested from ex situ experiments⁷, but which has been questioned recently⁸.

RESULTS AND DISCUSSION

Raman spectra of the glass and reaction product

Raman spectroscopy on silicate glasses provides insights into its structural network organization, mainly on the connectivity of Si–O bonds. The degree of polymerization is reflected by the distribution of Q^n species in the amorphous structure, where Q^n depicts a silica tetrahedron and n the number of linkages over the oxygen corners to adjacent SiO_4 tetrahedra. With $n = 0$ (Q^0), the tetrahedron is fully isolated from the remaining silica network, sharing no corner with another silica tetrahedron. On the other side, Q^4 represents a four-corner-shared tetrahedron in a three-dimensional silicate network. The connectivity of Q^n species is also referred to as the number of non-bridging oxygens (NBO), whereby a bridging oxygen being the corner- or edge shared

oxygen(s) of adjacent tetrahedrons. An NBO may be connected to glass network modifiers (e.g., Na^+) within the glass or interacting with an atmosphere or solution at the glass surface.

Figure 2 includes a Raman spectrum of the pristine ternary Na borosilicate glass with O–Si–O bending and Si–O stretching modes in the spectral range from 200 to 2800 cm^{-1} , second-order bands²⁵ between 2400 and 2800 cm^{-1} . Furthermore, the ν_5 symmetric B–O stretching modes of planar metaborate ring structures²⁶ were detected near 630 cm^{-1} and the symmetric stretching modes of the above-mentioned Q^n species between 900 and 1250 cm^{-1} , with the Q^3 having the highest intensity. Bond vibrations of BO_3 units in boroxol rings and the stretching bands of molecular oxygen (1555 cm^{-1}) and nitrogen (2331 cm^{-1}) from air between objective and glass surface were also detected. While the occurrence of Q^n species can be expected within the spectral range between 850 and 1250 cm^{-1} , an exact band assignment for each Raman spectrum was tested, but finally not performed due to the too low signal-to-noise ratio and complex background of the individual spectra. However, a quantitative approach for the pristine glass (and an heavy ion irradiated counterpart) can be found elsewhere²⁷. In particular, the chemical composition of borosilicate glasses is the major control on the degree of polymerization of the glass network, which is reflected by the Raman intense Q^n bands. However, for the amorphous silica, which is the main reaction product observed in this study, the increase in polymerization is best seen in the increase of siloxane ring sizes observed by the symmetric ring-breathing mode vibrations (δ_{breath}) in the low wavenumber region (Fig. 2) as the intensity of the Q^n speciation is comparatively low. In detail, the spectrum of the here found amorphous silica is generally characterized by a red-shifted, sharp D_1 band around 490 cm^{-1} attributed to fourfold siloxane rings. The absence of the D_2 band indicates that smaller, i.e., threefold siloxane rings are neglectable or did not occur. The overall band profile exhibits an asymmetry, which can be attributed to siloxane rings of higher orders (\geq fivefold)²⁸. As expected, modes of the metaborate ring structures found in the pristine glass cannot be observed in the amorphous silica, but further Si–O–Si bending modes are observed between 750 and 850 cm^{-1} . The symmetric stretching modes (ν_s) of the Q^n species are detected, but are overlain by a sharp intense band near 975 cm^{-1} , which can be attributed to the symmetric stretching mode of the Si–O bond of silanol groups^{28,29}. In the higher wavenumber region, the typical OH and H_2O vibrational modes of water and surface silanol groups can be seen (Fig. 2). A summary of the important vibrational modes in the measured spectral range for amorphous silica can be found in Table 1.

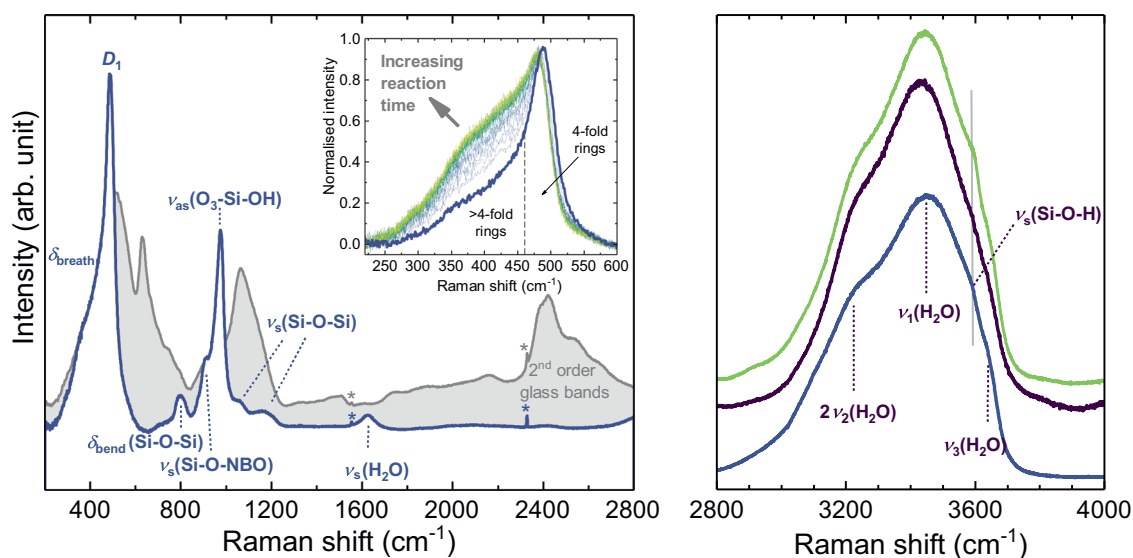


Fig. 2 Structural changes in amorphous silica. Representative background-corrected Raman spectra from amorphous silica (blue spectrum) formed within the first hours of the experiment near the glass surface, and from the silicate glass (light grey spectrum), showing the typical glass bands with second-order bands between 2300 and 2900 cm^{-1} . Raman modes for silica are assigned after Aguiar et al.²⁸. The stars (*) mark bands from O_2 (1555 cm^{-1}) and N_2 (2331 cm^{-1}) of the air between glass and objective. Inset diagram shows a series of Raman spectra in the frequency range between 200 and 600 cm^{-1} that were taken at different times at the same location (cf. Fig. 3a). The blue and yellow spectra represent the first and last measurement at that location, respectively. Note that with increasing reaction time, the intensity near 430 cm^{-1} increases significantly, reflecting the formation of five- and sixfold silica rings with time. Moreover, the $\nu_s(\text{Si-O-H})$ band is not visible in all spectra (purple spectrum), indicating an inhomogeneous distribution of silica inner surface OH groups that are linked via hydrogen to a water molecule (cf. Fig. 3b).

Table 1. Overview of relevant Raman modes found in amorphous silica.

Raman shift (cm^{-1})	Mode	Description
430	$\delta_{\text{breath}}(\text{Si-O-Si})$	Symmetric breathing modes of ≥ 5 -fold Si-O-Si rings ^a
450–490	$\delta_{\text{rock}}(\text{Si-O-Si})$	Silica rocking bands ^a
488–495	D_1	Defect band = symmetric breathing modes of planar fourfold Si-O-Si rings ^{ab}
601	D_2	Defect band = symmetric breathing modes of planar threefold Si-O-Si rings ^a
783–837	$\delta_{\text{bend}}(\text{Si-O-Si})$	Silica bending bands ^a
860	$\nu_{\text{as}}(\text{O}_2\text{Si}=\text{NBO}_2)$	Asymmetric stretching of Q^{2a}
967–970	$\nu_{\text{as}}(\text{O}_3\text{Si}-\text{NBO})$	Asymmetric stretching modes of Q^3
	$\nu_{\text{as}}(\text{O}_3\text{Si}-\text{OH})$	Asymmetric stretching of Si-O in surface silanol groups ^c
1060–1170	$\nu_s(\text{Si-O-Si})$	Si-O-Si stretching modes ^a
~1630	$\nu_2(\text{H}_2\text{O})$	Bending mode of 'free' water and water H-bonded to H^+ of silanol group ^c
3250	$2\nu_2(\text{H}_2\text{O})$	First overtone of water bending mode ^d
3450	$\nu_1(\text{H}_2\text{O})$	Symmetric stretching mode of water ^d
3520		Superimposition of OH vibrations of adsorbed water molecules and vicinal/geminal silanol groups ^d
3610	$\nu_3(\text{H}_2\text{O})$	Asymmetric stretching mode of water ^d
3615	$\nu_s(\text{SiO-H})$	Stretching mode of silanol groups (H-bonded to O of water) ^c
~3680	$\nu_s(\text{Si-OH})$	Stretching mode of vicinal/geminal silanol groups ^a
3750	$\nu_s(\text{Si-OH})$	Stretching mode of isolated silanol groups ^a

Spectral assignments after ^aAguiar et al.²⁸, ^bGaleener⁵⁵, ^cDavis and Tomozawa⁵⁶, ^dAnedda³⁰.

To study the structural changes of the precipitated amorphous silica in space and time, a band intensity ratio has recently been defined²⁴ that allows monitoring the polymerization of the amorphous silica. For this, the integrated intensity of the δ_{breath} symmetric breathing modes of fivefold and higher siloxane ring structures between 250 and 460 cm^{-1} was divided by the total integrated breathing mode intensity from all siloxane ring

structures measured between 250 and 600 cm^{-1} (R_r , see Table 1) after subtraction of a cubic background. In addition, in this study also the relative fraction of adsorbed water onto the amorphous silica was determined by the ratio of the integrated intensity between 3500 and 3550 cm^{-1} , where the superimposed OH vibrations of adsorbed water molecules and vicinal/geminal silanol groups³⁰ are found, over the integrated intensity of the

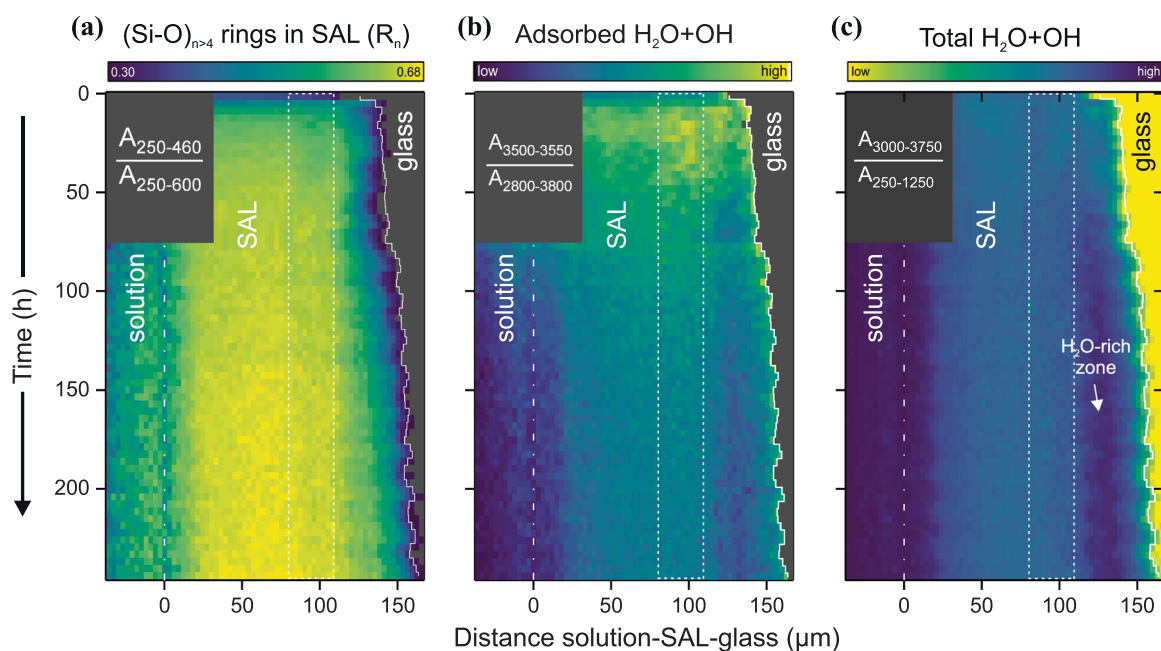


Fig. 3 Spatial and temporal evolution of the surface alteration layer. False-colour Raman images rendered from the recorded spectra over time, showing the spatial distribution of **(a)** the relative fraction of five- and sixfold rings in silica, **(b)** the relative fraction of adsorbed water on the silica surface, and **(c)** OH groups in the analysed volume. The images were obtained by colour-coding the ratios $A_{250-460}/A_{250-600}$, $A_{3500-3550}/A_{2800-3800}$, and $A_{3000-3750}/A_{250-1250}$, where A represents the accumulated and background-corrected intensity in the frequency range given as index (in cm^{-1}). Dashed lines encase profile location shown in Fig. 4, white lines represent the location of the retreating silica/glass interface, which is derived from sigmoidal fits of the intensity of the OH bands. Grey areas in the top-left were initially not imaged. Glass areas in **(a)** and **(b)** are also shown in grey as the selected regions of integrated Raman band intensities are not directly applicable for glass.

total $\text{H}_2\text{O}/\text{OH}$ bands measured between 2800 and 3800 cm^{-1} (Fig. 2). Moreover, the relative fraction of (solely) surface silanol groups in the amorphous silica was estimated from the ratio of the integrated intensity of the sharp Si–OH band between 935 and 1010 cm^{-1} over the surrounding vibrational modes of the Q^n species of silica between 850 and 1250 cm^{-1} (Fig. 2). Lastly, the relative content of water species in the analysed volume was determined by the ratio of the integrated intensity of the OH groups measured between 3000 and 3750 cm^{-1} and the integrated intensity of the intense silica vibrational modes measured between 250 and 1250 cm^{-1} . Note that all these parameters are not a correct quantitative measure of the actual fractions. In the absence of a detailed understanding of the silica structure and its Raman spectrum, however, these ratios are easily determinable parameters that can be used to monitor relative structural changes in silica as a function of space and time, which is relatively independent of spectrum quality and physical assumptions. As such, this approach has proven to be a robust method to analyse the large number of about 5000 Raman spectra collected during the experiment.

Corrosion dynamics

By the time the first mapping step was finished (1 + 1 h experimental setup + imaging), an hydrous amorphous silica layer of about $90\text{ }\mu\text{m}$ had already formed (Fig. 3c). The formation progress of this SAL could therefore not be followed directly. Note here that the initial reaction surface has not been polished extensively due to the fabrication process of the cell lid. It appears to be an inherent disadvantage of the lid redesign due to the technical challenges to properly polish the inside of the blind hole. This could be a reason for the observed extremely high reactivity at the start of the experiment. However, solid-state diffusion processes in borosilicate glasses in this temperature regime are rather slow as revealed by ToF-SIMS analyses, showing that

hydrogen diffuses merely a few tenths of micrometres within 209 days¹⁴. It can therefore be ruled out that a diffusion-controlled glass hydrolysis and ion exchange process has produced such a thick layer within 2 h. Accordingly, it is very likely that even under acidic bulk conditions the SAL precipitated from solution by an ICDP process as suggested previously⁷. Hereby, the congruent dissolution releases glass constituents into solution, with the possibility of saturating the adjacent solution at the solution–glass interface with respect to amorphous silica, especially in the case of acidic (to low-alkaline) solutions, where overall silica solubility is very low, i.e., in the order of 150 ppm^4 . Moreover, the solution volume within the drilled blind hole may be saturated much faster than the underlying bulk solution (Fig. 1). Such local silica saturation at a dissolving interface was also observed in experiments on the replacement of wollastonite by amorphous silica²³. The principle idea behind local saturation in a surface boundary solution is that during dissolution a concentration gradient between bulk solution and dissolving interface will develop if the release rate of Si from the glass is higher than the transport of Si into the bulk solution. This is particularly relevant within cracks, where supersaturation is much faster reached than at surfaces in contact with the bulk solution. In the wollastonite study, the interfacial solution also showed a distinctively higher pH value than the surrounding solution (due to the release of calcium by the dissolution of wollastonite). For the borosilicate glass used here, we previously found with the help of relative changes in the carbonate speciation also a pH gradient in front of the water–SAL interface (and also further within the SAL)²⁴. Due to the pH condition used here, we cannot determine the pH in this experiment, but the release of sodium from the glass into the interfacial solution should have also increased the local pH. An increase in pH, however, only effectively changes the solubility of amorphous silica if the pH is higher than about 9 at $70\text{ }^\circ\text{C}$, but shifts the polymerization of silica into the domain of rapid

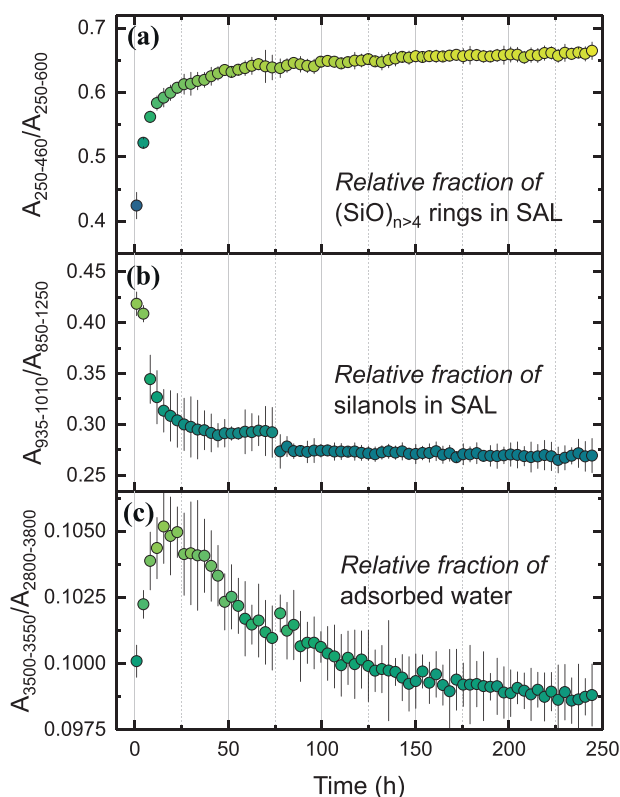
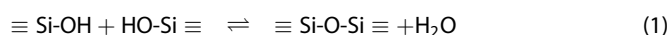


Fig. 4 Structural changes in the SAL over time. Time dependence of the ratios (a) $A_{940-1000}/A_{750-1250}$, (b) $A_{250-460}/A_{250-600}$, and (c) $A_{3560-3620}/A_{3000-3750}$ taken from the locations enclosed by the dashed lines (average over 10 pixel) in Fig. 3. Errors bars reflect the two-sigma errors.

aggregation (pH 2–7)⁴. Hence, nanoparticles of silica from the condensation of monomeric silicic acid to dimers and oligomers/cyclic structures in solution would quickly cross-link to form a gel through the ongoing reaction of silanol groups to siloxane bridges represented by the following equation:



The aggregation of particles is particularly preferred in the presence of sodium, which neutralizes the negative surface charge of silica particles⁴. Within the next 10 h, the hydrous silica gel polymerized and aggregated, which is indicated by a red-shift of the D_1 band at the very beginning and the strong increase in Si–O–Si ring structures of higher orders (Figs. 2 and 3a). At the same time, the ratio of surficial silanol groups in the SAL to silica bound in the network of the silica particles decreased in an anti-correlated fashion (Fig. 4). The number of surficial silanol groups and the resulting capability to adsorb water molecules at the surface is a function of the surface properties, i.e. surface curvature and charge. The Raman band at 3520 cm^{-1} represents a superimposition of silanol-related vibrations: (1) O–H vibrations of water molecules adsorbed at the surface and (2) geminal/vicinal silanols hydrogen-bonded to oxygen atoms of adjacent silanol groups and/or adsorbed water molecules (Table 1). According to Fig. 4, water adsorption by silica in the SAL increases in comparison to the overall water content of the SAL up to 25 h of the experiment, after which it declines again. A plausible explanation for this behaviour is the change of curvature during silica sphere growth, which results in the interaction of previously isolated silanol groups to, in turn, change the surface charge and attract free molecular water³¹. However, the growth of spheres changes the

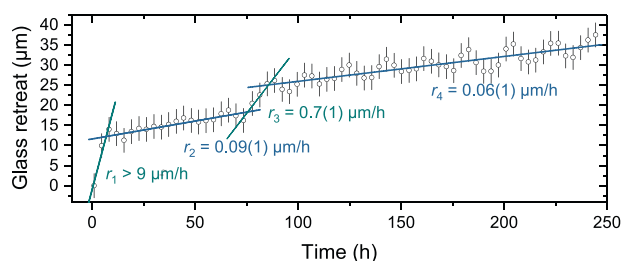


Fig. 5 Glass dissolution rate regimes. Retreat of the silica–glass interface as a function of time, showing four different kinetic regimes. The given rates r_2 , r_3 , and r_4 were obtained by a linear least-squares fit to the data. However, r_1 was estimated considering that a $\sim 90\text{-}\mu\text{m}$ -thick silica had already formed before the first image was taken. The glass retreat is given by the shift of the position of silica–glass interface compared to its position in the first image at $t = 1.0 \text{ h}$. The undulation on the fitted position is an artefact of the mechanical x – y – z table. Errors bars reflect the two-sigma errors.

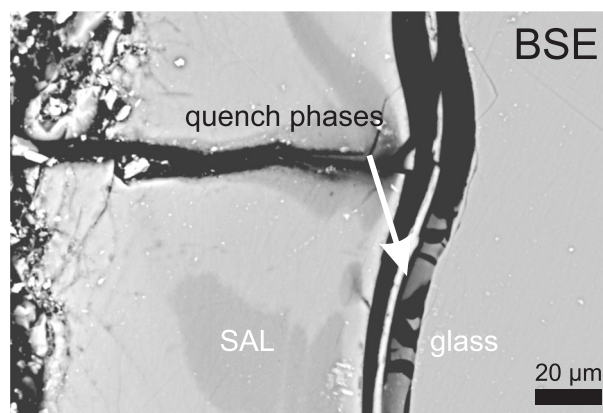


Fig. 6 Gap formation. Backscattered electron image taken after the experiment from a polished section that was prepared from the dried glass window. Note the occurrence of a gap/crack marking the interface between the pristine glass and the SAL.

surface to volume ratio, which decreases the concentration of surficial silanol groups in the sampling volume of the laser beam³². For a more detailed discussion on this mechanism of water adsorption see the Supplementary Note 1. Note that the agglomeration of small silica particles, i.e. gelling, also changes surface properties and might enhance water adsorption in parallel to sphere growth by the capillary effect³³.

After about 75 h, when the initial maturation progress levels out (Fig. 4), a water-rich zone between the pristine glass and SAL formed (Fig. 3c), as indicated by the ratio of the integrated intensities of the OH bands over the lower spectral range of the solid silica ($A_{3000-3700}/A_{250-600}$). At this stage, a dramatic increase in the retreat rate of the glass interface has been observed for about 15 h (Fig. 5), during which the water-rich zone apparently grew at the expense of the pristine glass.

The different corrosion rates, estimated here by the in situ measured glass retreat (Fig. 5), correlate well with the established rate regimes^{1,34}. The initial rate, r_1 (Fig. 5), corresponds to the fast forward dissolution rate (Stage I⁶), which is evoked by the congruent dissolution of the glass network^{3,7}. The slowdown of the corrosion rate by about two orders of magnitude after the formation of the initial SAL (r_2 , Fig. 5) conforms with the residual rate regime (Stage II⁶). Hereby, the rate is controlled by the transport properties of the SAL³. In the literature, a later-stage resumption of the corrosion rate was reported and proposed to

originate from the rapid formation of secondary minerals like phyllosilicates and zeolites at solution–silica interface^{35–37}, which are supposed to cause an undersaturation of the (local) solution and a destabilization of the gel layer^{38,39}. However, the formation of secondary phases was not observed during (Fig. 3a–c) or after (Fig. 6) the here presented *in situ* data. The glass composition does not support the formation of secondary mineral phases like phyllosilicates and zeolites. Nonetheless, a short resumption of the corrosion rate was observed (r_3 , Fig. 5), which here correlates with the formation of the water-rich zone at the SAL–glass interface (Fig. 3c). A plausible explanation for this is an increase in pH at the silica–glass interface caused by release of Na from the congruent glass dissolution and the transport limitation through the polymerized SAL. As such, the interfacial (pore) solution could have been undersaturated with respect to amorphous silica and might have temporarily increased the rate of congruent glass dissolution, after which the corrosion rate dropped again down to a residual rate, r_4 (Fig. 5).

After the experiment was terminated, the gap between the pristine glass and the SAL could clearly be observed in back-scattered electron (BSE) images (Fig. 6). This gap likely represents the water-rich zone observed during the experiment. Quenching and drying caused the precipitation of hydrous amorphous silica that partly fills the gap (dark-grey in the BSE image). The areas of darker BSE intensity in the inner parts of the SAL can be attributed to residual water in the silica structure. We note that the width of the gap is about 20 μm , which is comparable to the water-rich zone observed *in situ*.

Implications

The above described observations into the dynamics of borosilicate glass corrosion in an initially acidic aqueous medium were only made possible by application of the *in operando* Raman technique and provide a series of insights needed to refine existing corrosion models. The most intriguing feature of glass corrosion found in this study might be the development of a water-rich zone at the interface between glass and SAL despite the low pH of the bulk solution. Gaps or cracks between pristine glass and reaction rim are commonly found in dried samples from *ex situ* experiments^{3,7,40–42} and are explained by cracking or ripping apart due to shrinkage of the hydrous silica layer. However, in this study and our previous *in operando* study²⁴, a gap formed already during the experiments in form of a water-rich zone of similar extend and is thus part of the corrosion process rather than a by-product of sample treatment. The formation of a water film at the reaction interface is a common phenomenon and fundamental feature of mineral replacement reactions by an ICDP^{43,44} that has been discussed to be also applicable to glass corrosion^{3,7,11,12,24}. Furthermore, the water-rich zone, being a structural weakness, could explain the phenomenon called ‘flaking’, ‘scaling’ or ‘delamination’, which is often observed in archaeological⁴⁵ and pharmaceutical glasses⁴⁶.

For glass corrosion at pH values higher than about 9, i.e., when silica solubility increases drastically, the ICDP mechanism has already been accepted^{8,14}. The results of this study do not only confirm the previously made observation and interpretation of the *in situ* gap formation under neutral to slightly alkaline conditions, but also provide further evidence that the ICDP mechanism also works under acidic conditions⁷.

Comparing the Raman spectra of the amorphous silica here with those from the previous *in operando* study, the intense D_1 band, representing fourfold silica rings, is only observed in this study. However, the effect of pH on the silica network formed from solution is well known⁴, and is here interpreted as further evidence that the SALs observed in our studies must be precipitated from solution principally over the entire pH range.

The development of the water-rich zone also shows a strong correlation with structural maturation of the SAL, which involves an increasing polymerization and silica sphere size growth, reflected by the relative decrease of surface-adsorbed water molecules (Fig. 4). Such maturation might slow down mass transport through the SAL, although water can readily transverse the SAL at such stage as indicated by deuterium tracer experiments²⁴. Depending on the ratio between glass corrosion rate and mass transport, the pH can increase in the (pore) solution and at the glass interface by continuous release of sodium from the glass. This, in turn, self-enhances the corrosion rate as could be observed by the (sudden) increase of the corrosion rate, which is not an uncommon phenomena and currently discussed issue in the nuclear waste glass community^{34,37,47}.

Finally, the fast formation of an SAL of about 90 μm within the first 2 h of the experiment is further evidence that the glass corrosion proceeds by an ICDP mechanism^{3,7,11,24} and that this process must not be restricted to high alkaline conditions as recently proposed⁸. Solid state diffusion-controlled hydrolysis and ion exchange reactions cannot facilitate glass corrosion over such a length scale within the short time frame of our experiment. However, it cannot be ruled out from this study whether the proposed corrosion mechanism is applicable to more complex glass compositions. In a recent study, the addition of Al to a similar ternary borosilicate glass significantly decreased the initial and residual glass dissolution rates in comparison to their Al-free glass⁴⁸. In which ways the glass composition and its resulting effects on the nearby reaction solution influences the identified individual reaction features, e.g., bond breakage of the silica network or silica saturation and growth, and thereby the overall reaction mechanism remains an issue that needs to be addressed in future studies. For this, long-term *in situ* experiments with more complex glasses could help to decipher whether a single mechanism is dominating over the entire compositional and pH range, in which dissolution, transport, polymerization, and precipitation rates change interdependently as a function of the local physico-chemical conditions. Solving this intricate interplay is a prerequisite for forward-modelling of glass corrosion rates.

METHODS

Glass sample

The glass was synthesized in a platinum crucible at 1400 °C for 3 h from SiO_2 , B_2O_3 , and Na_2CO_3 powder that was mixed in the proportion to reach a target glass composition of 60 mol% SiO_2 , 20 mol% Na_2O , and 20 mol% B_2O_3 . The glass was molten a second time after crushing and milling it in a ball mill to ensure chemical homogeneity. After quenching the melt in a pre-heated stainless steel mold, it was tempered at ~ 560 °C for 6 h, letting it cool down by switching off the oven. The monoliths were stored in closed glass bottle at room temperature and show no observable corrosion by naked eye until present. The lid was prepared by cutting a $10 \times 10 \times 5$ mm³ large piece from the raw glass monolith. An approximately 4 mm deep and 5 mm wide blind hole was then drilled into the centre of the glass plate using a diamond drill. To minimize surface roughness, the internal surface was polished with 3 μm diamond paste on a cotton bud, which was attached to a handheld drilling machine. All faces were then carefully ground and polished, reducing the bottom of the blind hole to a thickness of 180 ± 10 μm . The lid was then used immediately. After the experiment, the glass sample was washed with distilled water and dried at 60 °C over night. To avoid Raman scattering from epoxy resin in the sample, the hole was stabilized by injecting a dense gypsum paste for grinding and polishing.

Experimental setup

For the *in operando* experiment, we redesigned the lid of our fluid cell²⁴ such that the borosilicate glass under investigation directly acts as the lid of the cell (Fig. 1). The blind hole in the centre of the lid, with the window sealing the cell at the top, permits measuring the initially pristine glass, the

emerging SAL, and the surrounding solution in a horizontal section across the glass hole wall as schematically shown in Fig. 1. This geometry provides a higher spatial resolution in direction of the reaction front movement than conventional confocal depth profiling. As corrosion agent a 0.1 M HCl solution with a pH of 1 at room temperature was chosen, since it is known from previous experiments with this glass composition that a several tenth of micrometre-thick SAL will form within a few days^{18,42}. The fluid cell was in this experiment only heated to 70 °C to not rupture the fragile glass window by the autogenous pressure. Over the course of the experiment, the pH increased to a value of 7.9 due to the release of sodium (and boric acid) from the glass into the solution as measured at the end of the experiment. Note here that the blind hole can be considered as a wide crack in which supersaturation of silica may occur earlier than in the underlying bulk solution.

Raman spectroscopy

The measurement were carried out with an Horiba Scientific HR800 Raman spectrometer equipped with an Olympus BX41 microscope in 180° backscatter geometry and a solid-state Nd:YAG laser ($\lambda = 532.08$ nm) as excitation source at the Institute of Geosciences at the University of Bonn, Germany. The scattered Raman light was collected in the frequency range between 200 and 4000 cm^{-1} by an Peltier-cooled electron-multiplier charge-coupled device detector, having a low thermal and read-out noise and high quantum efficiency, after having passed through a 500 μm confocal aperture and a 100 μm spectrometer entrance slit and being dispersed by a grating of 600 grooves/mm. With this analytical setup the spectral resolution was 3.5 cm^{-1} , as given by the full-width at half-maximum of Ne lines. The accuracy of the spectrometer was monitored by the O₂ and the N₂ band from the air between glass and objective at 1555 and 2331 cm^{-1} , respectively (Fig. 1b). The intensities were corrected for the overall instrument response function (known as white light correction). After filling the fluid cell with the solution and closing it with the glass lid, the cell was placed on a motorized x–y–z stage of the Raman spectrometer with a step size of 0.1 and 0.5 μm in x, y, and z direction, respectively, and heated to 70 ± 5 °C. A LWD ×100 objective with a numerical aperture, NA, of 0.8 and a working distance of 3.4 mm was used. Since the glass water interface could not be seen in optical images, the interface was initially searched by measuring the OH frequency region between 2800 and 4000 cm^{-1} and scanning in x–y–z direction. About 1 h was needed to find the optimal analytical position and parameters for the measurements. The progress of the corrosion was measured at a depth of ~250 μm below the glass surface, where the spatial resolution is naturally several orders worse than the resolution close to the surface. By fitting a Boltzmann function to the integrated intensities of the OH bands across individual line scans, a lateral resolution of 10.2 ± 2.2 μm (2 s.d.) was estimated empirically. The decrease of lateral resolution with depth mainly reflects the dramatic decrease of the refraction-limited depth resolution, i.e., the dramatic increase of the length of the region illuminated by the incoming laser beam. This length depends mainly on NA and the refraction index of the glass and can reach several tenth of micrometres when focusing deep into the sample^{49–51}.

The x–y dimension of the imaged area was initially 135 × 7.5 μm^2 with pixel spacing of 3.0 and 2.5 μm in x and y direction, respectively, but was increased to 250 × 7.5 μm^2 after about 77 h using the same pixel spacing. The imaged area was increased, because it was realized that it did not extend into the solution and pristine glass at the same time, because a several micrometre-thick OH-rich silica zones had already developed unexpectedly within the first hour. The beam power was initially set to ~430 mW at the surface of the glass lid, but was then increased to ~610 mW to compensate for lower count times per pixel over an enlarged imaging area. The total counting time per pixel of an image was initially 30 times for 1 s, but was decreased to 20 times 0.7 s, yielding total image acquisition times of ~70 and 60 min, respectively. Altogether, 68 x–y images were collected within about 250 h.

Data reduction

All Raman spectra were corrected for temperature effects and wavelength dependence of the scattering process⁵²,

$$I = I_{\text{obs}} \cdot \nu_0^2 \cdot \left[1 - \exp\left(\frac{-h\nu}{kT}\right) \right] \frac{\nu}{(\nu_0 - \nu)^3} \quad (2)$$

where I_{obs} is the measured intensity (in counts/s), h is the Planck constant, c is the speed of light, k is the Boltzmann constant, T is the absolute

temperature (in K), ν_0 is the wavenumber of the incident laser beam (in cm^{-1}), and ν is the measured wavenumber (in cm^{-1}). See also Neuville et al.⁵³ or Behrens and Mysen⁵⁴ for the application of the Long correction⁵². The spectral analyses were then performed in the typical frequency regions of O–Si–O bending and Si–O stretching modes, as well as of OH stretching vibrations: (1) 200–600 cm^{-1} , (2) 750–1100 cm^{-1} , and (3) 2800–4000 cm^{-1} . In these frequency regions a cubic background was first subtracted and the integrated intensities were determined for the bands of interest by summing up the intensity multiplied by the spectral width within a certain frequency region using the LabSpec 6 software. Due to imaging misalignment, missing data points between 30 < x < 75 and 65 < t < 77 μm had to be interpolated by an Akima spline (fitted in y-direction (time)). Deconvolution of the spectral regions by least-squares fitting of spectroscopic functions to the experimental profiles was not performed, since intensity integration appeared more robust as no physical model is needed to fit the multitude of overlapping vibrational modes (Fig. 2). For visualization of the four-dimensional x–y–t intensity space of the recorded spectral maps (Fig. 3), the first of three lines in x-direction ($y = -2.5$) per time step was chosen (as x–y-mapping was performed first in x- and then y-direction).

Electron microprobe

A Jeol Superprobe 8200 at the Institute of Geosciences at the University of Bonn, Germany, was used to image the corroded glass after the experiment. Therefore, the fragile SAL inside the blind hole was stabilized with gypsum paste. After drying, the glass lid was cross-sectioned and grind down and to about the height of the Raman imaging plane, followed by polishing steps with 3 and 1 μm diamond spray. The sample was then coated with carbon and imaged with SE and BSE detectors.

DATA AVAILABILITY

All data that support the findings of this study are available from the corresponding author upon reasonable request.

CODE AVAILABILITY

All scripts for data treatment in this study are available from the corresponding author upon reasonable request.

Received: 18 November 2020; Accepted: 8 June 2021;
Published online: 09 July 2021

REFERENCES

- Frugier, P. et al. SON68 nuclear glass dissolution kinetics: current state of knowledge and basis of the new GRAAL model. *J. Nucl. Mater.* **380**, 8–21 (2008).
- Rebiscoul, D., Frugier, P., Gin, S. & Ayrat, A. Protective properties and dissolution ability of the gel formed during nuclear glass alteration. *J. Nucl. Mater.* **342**, 26–34 (2005).
- Geisler, T. et al. The mechanism of borosilicate glass corrosion revisited. *Geochim. Cosmochim. Acta* **158**, 112–129 (2015).
- Iler, R. K. *The Chemistry of Silica: Solubility, Polymerization, Colloid and Surface Properties and Biochemistry of Silica* (Wiley, 1979).
- Vernaz, E., Gin, S., Jégou, C. & Ribet, I. Present understanding of R7T7 glass alteration kinetics and their impact on long-term behavior modeling. *J. Nucl. Mater.* **298**, 27–36 (2001).
- Gin, S. Open scientific questions about nuclear glass corrosion. *Procedia Mater. Sci.* **7**, 163–171 (2014).
- Geisler, T. et al. Aqueous corrosion of borosilicate glass under acidic conditions: a new corrosion mechanism. *J. Non-Cryst. Solids* **356**, 1458–1465 (2010).
- Gin, S. et al. The fate of silicon during glass corrosion under alkaline conditions: a mechanistic and kinetic study with the International Simple Glass. *Geochim. Cosmochim. Acta* **151**, 68–85 (2015).
- Gin, S. et al. Origin and consequences of silicate glass passivation by surface layers. *Nat. Commun.* **6**, 6360 (2015).
- Verney-Carron, A. et al. Understanding the mechanisms of Si–K–Ca glass alteration using silicon isotopes. *Geochim. Cosmochim. Acta* **203**, 404–421 (2017).
- Lenting, C. et al. Towards a unifying mechanistic model for silicate glass corrosion. *npj Mater. Degr.* **2**, 28 (2018).
- Hellmann, R. et al. Unifying natural and laboratory chemical weathering with interfacial dissolution–reprecipitation: a study based on the nanometer-scale chemistry of fluid–silicate interfaces. *Chem. Geol.* **294–295**, 203–216 (2012).

13. Hellmann, R. et al. Nanometre-scale evidence for interfacial dissolution–reprecipitation control of silicate glass corrosion. *Nat. Mater.* **14**, 307–311 (2015).
14. Gin, S. et al. Atom-probe tomography, TEM and ToF-SIMS study of borosilicate glass alteration rim: a multiscale approach to investigating rate-limiting mechanisms. *Geochim. Cosmochim. Acta* **202**, 57–76 (2017).
15. Gratz, A., Manne, S. & Hansma, P. Atomic force microscopy of atomic-scale ledges and etch pits formed during dissolution of quartz. *Science* **251**, 1343–1346 (1991).
16. Putnis, C. V. & Ruiz-Agudo, E. The mineral–water interface: where minerals react with the environment. *Elements* **9**, 177–182 (2013).
17. Higgins, S. R., Eggleston, C. M., Knauss, K. G. & Boro, C. O. A hydrothermal atomic force microscope for imaging in aqueous solution up to 150 °C. *Rev. Sci. Instrum.* **69**, 2994–2998 (1998).
18. Donzel, N., Gin, S., Augereau, F. & Ramonda, M. Study of gel development during SON68 glass alteration using atomic force microscopy. Comparison with two simplified glasses. *J. Nucl. Mater.* **317**, 83–92 (2003).
19. Abraitis, P. K. et al. The kinetics and mechanisms of simulated British Magnox waste glass dissolution as a function of pH, silicic acid activity and time in low temperature aqueous systems. *Appl. Geochem.* **15**, 1399–1416 (2000).
20. Lutge, A. & Arvidson, R. S. Reactions at surfaces: a new approach integrating interferometry and kinetic simulations. *J. Am. Ceram. Soc.* **93**, 3519–3530 (2010).
21. Icenhower, J. P. & Steefel, C. I. Dissolution rate of borosilicate glass SON68: a method of quantification based upon interferometry and implications for experimental and natural weathering rates of glass. *Geochim. Cosmochim. Acta* **157**, 147–163 (2015).
22. Wild, B. et al. Physical properties of interfacial layers developed on weathered silicates: a case study based on labradorite feldspar. *J. Phys. Chem. C* **123**, 24520–24532 (2019).
23. Ruiz-Agudo, E. et al. Control of silicate weathering by interface-coupled dissolution–precipitation processes at the mineral–solution interface. *Geology* **44**, 567–570 (2016).
24. Geisler, T., Dohmen, L., Lenting, C. & Fritzsche, M. B. K. Real-time in situ observations of reaction and transport phenomena during silicate glass corrosion by fluid-cell Raman spectroscopy. *Nat. Mater.* **18**, 342–348 (2019).
25. To, T. T., Bougeard, D. & Smirnov, K. S. Molecular dynamics study of the vibrational pattern of ring structures in the Raman spectra of vitreous silica. *J. Raman Spectrosc.* **39**, 1869–1877 (2008).
26. Wu, K. & Lee, S.-Y. Ab initio calculations on normal mode vibrations and the Raman and IR spectra of the [B3O6] 3-metaborate ring. *J. Phys. Chem. A* **101**, 937–940 (1997).
27. Lönart, M. I. et al. The effect of heavy ion irradiation on the forward dissolution rate of borosilicate glasses studied in situ and real time by fluid-cell Raman spectroscopy. *Materials* **12**, 1480 (2019).
28. Aguiar, H., Serra, J., González, P. & León, B. Structural study of sol–gel silicate glasses by IR and Raman spectroscopies. *J. Non-Cryst. Solids* **355**, 475–480 (2009).
29. Davis, K. & Tomozawa, M. Water diffusion into silica glass: structural changes in silica glass and their effect on water solubility and diffusivity. *J. Non-Cryst. Solids* **185**, 203–220 (1995).
30. Anedda, A., Carbonaro, C. M., Clemente, F., Corpino, R. & Ricci, P. C. Raman investigation of surface OH-species in porous silica. *J. Phys. Chem. B* **107**, 13661–13664 (2003).
31. Brinker, C. J. & Scherer, G. W. *Sol-Gel Science: The Physics and Chemistry of Sol-Gel Processing* (Academic Press, 1990).
32. Rahman, I., Vejayakumaran, P., Sipaut, C., Ismail, J. & Chee, C. Size-dependent physicochemical and optical properties of silica nanoparticles. *Mater. Chem. Phys.* **114**, 328–332 (2009).
33. Keskinen, H. et al. On-line characterization of morphology and water adsorption on fumed silica nanoparticles. *Aerosol Sci. Technol.* **45**, 1441–1447 (2011).
34. Frugier, P., Fournier, M. & Gin, S. Modeling resumption of glass alteration due to zeolites precipitation. *Procedia Earth Planet. Sci.* **17**, 340–343 (2017).
35. Gin, S. & Mestre, J. SON 68 nuclear glass alteration kinetics between pH 7 and pH 11.5. *J. Nucl. Mater.* **295**, 83–96 (2001).
36. Vienna, J. D., Ryan, J. V., Gin, S. & Inagaki, Y. Current understanding and remaining challenges in modeling long-term degradation of borosilicate nuclear waste glasses. *Int. J. Appl. Glass Sci.* **4**, 283–294 (2013).
37. Fournier, M., Gin, S. & Frugier, P. Resumption of nuclear glass alteration: state of the art. *J. Nucl. Mater.* **448**, 348–363 (2014).
38. Rajmohan, N., Frugier, P. & Gin, S. Composition effects on synthetic glass alteration mechanisms: Part 1. Experiments. *Chem. Geol.* **279**, 106–119 (2010).
39. Gin, S., Beaudoux, X., Angéli, F., Jégou, C. & Godon, N. Effect of composition on the short-term and long-term dissolution rates of ten borosilicate glasses of increasing complexity from 3 to 30 oxides. *J. Non-Cryst. Solids* **358**, 2559–2570 (2012).
40. Anaf, W. Study on the formation of heterogeneous structures in leached layers during the corrosion process of glass. In *CeROArt. Conservation, Exposition, Restauration d'Objets d'Art* (ed. Annys, E.) (CeROArt asbl, 2010).
41. Sterpenich, J. & Libourel, G. Using stained glass windows to understand the durability of toxic waste matrices. *Chem. Geol.* **174**, 181–193 (2001).
42. Dohmen, L. et al. Pattern formation in silicate glass corrosion zones. *Int. J. Appl. Glass Sci.* **4**, 357–370 (2013).
43. Putnis, A. Mineral replacement reactions: from macroscopic observations to microscopic mechanisms. *Mineral. Mag.* **66**, 689–708 (2002).
44. Putnis, A. & Putnis, C. V. The mechanism of reequilibration of solids in the presence of a fluid phase. *J. Solid State Chem.* **180**, 1783–1786 (2007).
45. Pearson, C. *Conservation of Marine Archaeological Objects* (Elsevier, 1988).
46. Guadagnino, E. & Zuccato, D. Delamination propensity of pharmaceutical glass containers by accelerated testing with different extraction media. *PDA J. Pharm. Sci. Technol.* **66**, 116–25 (2012).
47. Ribet, S. & Gin, S. Role of neoformed phases on the mechanisms controlling the resumption of SON68 glass alteration in alkaline media. *J. Nucl. Mater.* **324**, 152–164 (2004).
48. Gin, S. et al. A general mechanism for gel layer formation on borosilicate glass under aqueous corrosion. *J. Phys. Chem. C* **124**, 5132–5144 (2020).
49. Everall, N. J. Modeling and measuring the effect of refraction on the depth resolution of confocal Raman microscopy. *Appl. Spectrosc.* **54**, 773–782 (2000).
50. Everall, N. J. Confocal Raman microscopy: why the depth resolution and spatial accuracy can be much worse than you think. *Appl. Spectrosc.* **54**, 1515–1520 (2000).
51. Baldwin, K. & Batchelder, D. Confocal Raman microspectroscopy through a planar interface. *Appl. Spectrosc.* **55**, 517–524 (2001).
52. Long, D. A. *Raman Spectroscopy* (McGraw-Hill, 1977).
53. Neuville, D. R. & Mysen, B. O. Role of aluminium in the silicate network: in situ, high-temperature study of glasses and melts on the join SiO₂–NaAlO₂. *Geochim. Cosmochim. Acta* **60**, 1727–1737 (1996).
54. Behrens, H., Roux, J., Neuville, D. & Siemann, M. Quantification of dissolved H₂O in silicate glasses using confocal microRaman spectroscopy. *Chem. Geol.* **229**, 96–112 (2006).
55. Galeener, F. Planar rings in glasses. *Solid State Commun.* **44**, 1037–1040 (1982).
56. Davis, K. & Tomozawa, M. An infrared spectroscopic study of water-related species in silica glasses. *J. Non-Cryst. Solids* **201**, 177–198 (1996).

ACKNOWLEDGEMENTS

We would like to thank the reviewers for valuable and constructive comments and suggestions. We are also grateful to the mechanical and electronics workshop of the Institute for Geosciences, University of Bonn, for the construction of the fluid cell. For financial support, we would like to acknowledge the German Research Foundation (grant no. GE1094/21-1 to T.G.) and the German Federal Ministry of Education and Research (BMBF) (within the joint research project 'ImmoRad—Fundamental investigations for the immobilization of long-lived radionuclides through interaction with secondary mineral phases in deep geological nuclear waste repositories', grant 02NUK019F to T.G.).

AUTHOR CONTRIBUTIONS

C.L. and T.G. conducted the experiment and analysed the data. C.L. wrote the first draft of the manuscript.

FUNDING

Open Access funding enabled and organized by Projekt DEAL.

COMPETING INTERESTS

The authors declare no competing interests.

ADDITIONAL INFORMATION

Supplementary information The online version contains supplementary material available at <https://doi.org/10.1038/s41529-021-00182-5>.

Correspondence and requests for materials should be addressed to C.L.

Reprints and permission information is available at <http://www.nature.com/reprints>

Publisher's note Springer Nature remains neutral with regard to jurisdictional claims in published maps and institutional affiliations.



Open Access This article is licensed under a Creative Commons Attribution 4.0 International License, which permits use, sharing, adaptation, distribution and reproduction in any medium or format, as long as you give appropriate credit to the original author(s) and the source, provide a link to the Creative Commons license, and indicate if changes were made. The images or other third party material in this article are included in the article's Creative Commons license, unless indicated otherwise in a credit line to the material. If material is not included in the

article's Creative Commons license and your intended use is not permitted by statutory regulation or exceeds the permitted use, you will need to obtain permission directly from the copyright holder. To view a copy of this license, visit <http://creativecommons.org/licenses/by/4.0/>.

© The Author(s) 2021